UNIVERSITY OF AMSTERDAM

UvA-DARE (Digital Academic Repository)

Magnetic Order and Superconductivity in Perovskites

Nugroho, A.A.

Publication date
2001

Link to publication

Citation for published version (APA):
Nugroho, A. A. (2001). *Magnetic Order and Superconductivity in Perovskites*. [, Universiteit van Amsterdam].

General rights
It is not permitted to download or to forward/distribute the text or part of it without the consent of the author(s) and/or copyright holder(s), other than for strictly personal, individual use, unless the work is under an open content license (like Creative Commons).

Disclaimer/Complaints regulations
If you believe that digital publication of certain material infringes any of your rights or (privacy) interests, please let the Library know, stating your reasons. In case of a legitimate complaint, the Library will make the material inaccessible and/or remove it from the website. Please Ask the Library: https://uba.uva.nl/en/contact, or a letter to: Library of the University of Amsterdam, Secretariat, Singel 425, 1012 WP Amsterdam, The Netherlands. You will be contacted as soon as possible.

UvA-DARE is a service provided by the library of the University of Amsterdam (https://dare.uva.nl)

Download date:11 Mar 2023

Chapter 4

Superconducting properties of $Nd_{1.85}Ce_{0.15}CuO_{4-\delta}$

4.1 Introduction

It has been widely accepted that the building blocks of the high-T_c superconductors consist of a superconducting block of antiferromagnetic CuO_2 layers and the charge reservoir block of the other oxides layer. The compound becomes superconductive when the antiferromagnetic layer is properly doped either by electrons or holes through a charge transfer from the charge reservoir block. The superconductivity in $Nd_{2-x}Ce_xCuO_4$ appears for $0.13 \leq x \leq 0.18$ after oxygen reduction, where x denotes the molar concentration of the dopant Ce. This superconductor is known as an electron-type superconductor because extra electrons instead of holes are supplied to the CuO_2 plane from the Ce-doped reservoir block. It is known that the highest T_c in this system is $\sim$ 24 K for x=0.15, although the corresponding oxygen content is rarely mentioned. This result has been reported for bulk as well as thin-film samples. Recently, Scavini et al. [1] showed that superconductivity in $Nd_{1.85}Ce_{0.15}CuO_{4-\delta}$ follows the 'universal relationship' between $T_c/T_{c,max}$ and the charge carrier content. The general picture for several series of the high-T_c compounds shows that the maximum T_c value is obtained for the number of carriers per Cu atom lying between 0.1 and 0.25. In this work, the investigation is focused only on the case of x=0.15 with the value for T_c of about 21 K. According to the 'universal relation' considered above, the number of carrier/Cu atom under investigation is about 0.08.

The superconducting as well as the normal state of this electron-type superconductor reveal a number of properties which are different from the other cuprate superconductors. Among these are the relatively moderate anisotropy ($\gamma = 200$) and the low T_c (T_c is between 21 and 24 K) which offer a special advantage for the study of a vortex state relatively free from the thermal fluctuation effect. Additionally, the transport and magnetic properties in the normal state ($T > T_c$) indicate a perceptible deviation from the linear dependency of the resistivity over an extended temperature range above T_c

with a higher residual resistivity ($\rho(T=0)$) in the range of 60 - 100 $\mu\Omega$-cm [3], a high resistivity ratio $\rho_c/\rho_{ab} \sim 10^4$, and a pronounced anisotropic contribution from the CF effects in the magnetic susceptibility.

It is well known that high-T_c superconductors have typical characteristic lengths which are different from those of the conventional low-T_c compounds. The shorter coherence length, ξ, and the larger penetration depth, λ, increase the value of the Ginzburg Landau parameter ($\kappa = \lambda/\xi$). Therefore, in high-T_c compound there is a lower critical field, $H_{c1} \sim \Phi_0 ln(\lambda/\xi)/\lambda^2$, where the vortices start to penetrate the superconductor, and a higher upper critical field, $H_{c2} \sim \Phi_0/\xi^2$, above which the superconductivity disappears ($\Phi_0 = hc/2e = 2.07$ x 10^{-7} G cm^2 is the flux quantum). The high T_c value enhances the role of thermal fluctuations near T_c which leads to the melting of the vortex lattice and to the existence of a vortex solid as well as a vortex liquid. Apart from the thermal fluctuations due to the higher T_c values, the layered structure of these compounds induces anisotropies in the vortex state and in other physical properties. In this layered superconductor, the supercurrent can flow either in the layer or between the layers, depending on the magnetic field direction, and thereby creating an Abrikosov vortex or a Josephson vortex, respectively.

Furthermore, the multi-element composition of the high-T_c compounds make them susceptible to structural disorder and defects which can also influence the anisotropy and modify the vortex structure. One of the interesting phenomena in connection with the disorder-induced vortex pinning effect is the appearance of a second peak in the shape of an arrow head in the magnetization curve. This so-called peak effect in the low-T_c compounds usually occurs in the vicinity of H_{c2} while it occurs generally at low field in the cuprate superconductors. Although some of the theoretical models for this phenomenon can explain the accumulating experimental data better than others, none of them alone provides a complete description of the effect. Even the more promising models are still subject to further experimental scrutiny.

In order to compare the superconducting state of $Nd_{1.85}Ce_{0.15}CuO_{4-\delta}$ with that of the other high-T_c compounds, the most important characteristics of this type-II superconductor are presented in this chapter. The Hao-Clem model [2, 4] is employed to estimate the Ginzburg-Landau (G-L) parameter κ, the critical field $H_{c2}(0)$, the coherence length $\xi_{ab}(0)$ and the penetration depth $\lambda_{ab}(0)$ in the dirty as well as the clean limit [5]. The vortex state of this compound is investigated by the isothermal magnetic hysteresis and the temperature dependence of the resistivity at various temperatures and magnetic fields. The results are summarized in a $H - T$ phase diagram. In addition, a more comprehensive phase diagram, incorporating the peak effect region in this compound, is also presented along with the results of analysis based on existing models [6]. For the study of the vortex dynamics involving the peak effect, the magnetic relaxation behavior is investigated in the entire range of magnetic fields covering the peak-effect region [7].

4.2 Characteristic length of $Nd_{1.85}Ce_{0.15}CuO_{4-\delta}$ derived from reversible magnetization

The Ginzburg-Landau (G-L) parameter, $\kappa = \lambda/\xi$, is one of the most important characteristics for type-II superconductors from a fundamental as well as a practical point of view. Before the advent of high-temperature copper-oxide superconductors, this parameter was commonly determined from the magnetization data M according to Abrikosov's formula derived from Ginzburg-Landau theory [8]

$$-4\pi M = \frac{H_{c2}(T) - H}{(2\kappa^2 - 1)\beta}, \tag{4.1}$$

where β is 1.16 for a hexagonal array. Eq.(4.1) is valid in the vicinity of H_{c2}. In the case of the high-T_c cuprate superconductors, most of the available magnetization data are limited to the field region far below H_{c2}, to which Eqs.(4.1) is not applicable. For these high-κ type-II superconductors, the characteristic behavior of the reversible magnetization in the broad intermediate-field region ($H_{c1} << H << H_{c2}$) is commonly described phenomenologically by the well-known formula derived from the London model [9],

$$-4\pi M = \frac{\Phi_o}{8\pi\lambda^2}\ln(\frac{\eta H_{c2}}{H}), \tag{4.2}$$

where η is a constant of order unity. Eq.(4.2) exhibits a linear dependence of M on $\ln(H)$. This description was initially found to agree reasonably well with the experimental results [10, 11, 12, 13].

A closer look at the derivation of Eq.(4.2) by Hao and Clem [2] has revealed, however, that the contribution of the core-energy term in the system's free energy density was ignored at derivation Eq.(4.2). Upon the inclusion of this additional term, the dimensionless G-L free energy per unit volume over a cross-sectional area A in a plane perpendicular to the vortices becomes [4]

$$F = \frac{1}{A}\int d^2\rho \left[\frac{1}{2}(1-f^2)^2 + \frac{1}{\kappa^2}(\nabla f)^2 + f^2(\mathbf{a} + \frac{1}{\kappa}\nabla\gamma)^2 + \mathbf{b}^2\right], \tag{4.3}$$

where f and γ are the normalized magnitude and phase of the order parameter $\psi = \psi_o f e^{i\gamma}$, with the vector potential $\mathbf{a}$ and the local magnetic flux density $\mathbf{b}$ satisfying the standard relations, $\nabla \cdot \mathbf{a} = \mathbf{0}$ and $\mathbf{b} = \nabla \times \mathbf{a}$. The dimensionless unit used in this chapter, corresponds to measuring the magnitude of the order parameter in units of Ψ_0, the length in units of λ, the magnetic field in units of $\sqrt{2}H_c = \kappa\Phi_0/2\pi\lambda^2$, the vector potential in units of $\sqrt{2}H_c\lambda = \kappa\Phi_0/2\pi\lambda$, and the energy in units of $H_c^2/4\pi$, where H_c is the thermodynamic critical field (Φ_0 corresponds to $2\pi/\kappa$ in the dimensionless expression).

An expression for the reversible magnetization is obtained by means of a variational calculation of F using the trial function

$$f = \frac{\rho}{(\rho^2 + \xi_\nu^2)^{1/2}} f_\infty, \tag{4.4}$$

where ρ is the radial coordinate measured from the vortex axis, while ξ_ν and f_∞ are the variational parameters, representing the effective core radius of the vortex and the depression of the order parameter due to the overlap of the vortices, respectively. For the isotropic case, the dimensionless reversible magnetization derived by this method from Eq.(4.3) is given by [4]

$$\begin{aligned} -4\pi M &= \frac{\kappa f_\infty^2 \xi_\nu^2}{2}\left[\frac{1-f_\infty^2}{2}\ln\left(\frac{2}{B\kappa\xi_\nu^2}+1\right) - \frac{1-f_\infty^2}{2+B\kappa\xi_\nu^2} + \frac{f_\infty^2}{(2+B\kappa\xi_\nu^2)^2}\right] \\ &+ \frac{f_\infty}{2\kappa\xi_\nu K_1(f_\infty\xi_\nu)}\left[K_0[\xi_\nu(f_\infty^2+2B\kappa)^{1/2}] - \frac{B\kappa\xi_\nu K_1[\xi_\nu(f_\infty^2+2B\kappa)^{1/2}]}{(f_\infty^2+2B\kappa)^{1/2}}\right] \\ &+ \frac{f_\infty^2(2+3B\kappa\xi_\nu^2)}{2\kappa(2+B\kappa\xi_\nu^2)^3}, \end{aligned} \tag{4.5}$$

where $K_n(x)$ is a modified Bessel function of the nth order. The magnetization M and the magnetic flux density B are related to the thermodynamic magnetic field H by the equation $B = H + 4\pi M$. Confining ourselves to high-κ cases ($\kappa > 10$), one has

$$f_\infty^2 = 1 - \left[\frac{B}{\kappa}\right]^4, \tag{4.6}$$

$$\left[\frac{\xi_\nu}{\xi_{\nu 0}}\right]^2 = \left[1 - 2\left(1-\frac{B}{\kappa}\right)^2\frac{B}{\kappa}\right]\left[1+\left(\frac{B}{\kappa}\right)^4\right], \tag{4.7}$$

with $\xi_{\nu 0} = \sqrt{2}/\kappa$.

It was shown in the same reference that the main features of the Abrikosov result can be recovered by this formula at high field. It was further suggested that an extension of this formula to the anisotropic case can be readily achieved by the introduction of an effective mass tensor or through the simple replacement of κ in Eqs.(4.5-4.7) by its average value $\bar{\kappa}$. This model has been applied successfully to the analysis of the reversible magnetization data of a $YBa_2Cu_3O_7$ single crystal [4], a c-axis-oriented bulk $Bi_2Sr_2Ca_2Cu_3O_8$ [14], a c-axis-oriented bulk $YBa_2Cu_4O_8$ [15], a polycrystalline bulk sample of $HgBa_2Ca_2Cu_3O_{8-x}$ [16], and a polycrystalline bulk sample of $Hg_{0.8}Pb_{0.2}Ba_{1.5}Sr_2Cu_3O_{8-x}$ [17]. Instead of its application to a high-T_c compounds, here we present the result is used by applying this model to the analysis of the reversible magnetization data of a low-T_c $Nd_{1.85}Ce_{0.15}CuO_{4-\delta}$ single crystal. This leads to the determination of its G-L parameter, κ, as well as the other thermodynamic parameters.

The high-quality single crystal of $Nd_{1.85}Ce_{0.15}CuO_{4-\delta}$ (NCCO) studied in this ex-

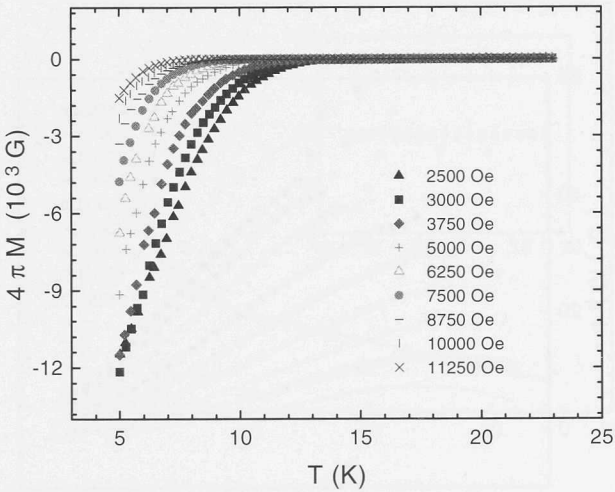

Figure 4.1: *Temperature dependence of the magnetization in various applied fields between 2500 and 11250 Oe parallel to the it c axis.*

periment was grown by the Traveling Solvent Floating Zone (TSFZ) technique using a four-mirror furnace as explained in chapter 2. As described there, the as-reduced crystal is superconducting at $T_c \sim 21$ K, with a transition width of $\Delta T_c \leq 1$ K as determined from its dc susceptibility curve measured by a commercial Quantum Design MPMS-5 magnetometer in a magnetic field of 10 Oe applied parallel to the c axis. The temperature dependence of the magnetization was also measured by the same magnetometer in various magnetic fields ranging between 2500 and 11250 Oe. The results of these measurements, after subtraction of the paramagnetic background, are presented in Fig. 4.1. Notice that the $M(T)$ curves do not exhibit crossover behavior typical for high-T_c copper-oxide superconductors as well as that revealed in the low-T_c $Sm_{1.85}Ce_{0.15}CuO_{4-\delta}$ (SCCO) [18] and $Pr_{1.85}Ce_{0.15}CuO_{4-\delta}$ (PCCO) [19]. The absence of thermal-fluctuation induced characteristics is apparently related to both the much lower T_c and the relatively moderate anisotropy of NCCO compared to the other systems mentioned above. It is further noted that each of the magnetization curves in Fig. 4.1 displays perceptible changes of slope over the entire range of measurement. Consequently, the data must be carefully chosen for their analysis on the basis of the theoretical description given by Eq.(4.5). Note that Eq.(4.5) is valid for specific temperatures and that the temperature dependence of M is hidden in B, which is normalized in units of $\sqrt{2}H_c(T)$. In this case, we restrict our $M-T$ data at each field only to those lying in a linear region (satisfying a linear fitting criterion of $R^2 = 0.99$) closest to T_c. These data turn out to be in the temperature range $11.25 \leq T \leq 19$ K as shown in Fig.4.2, and fall into the region of the vortex liquid state in the $H-T$ phase diagram presented in Ref.[5], and further confirmed by the ZFC-FC measurements above the irreversibility temperature T_{irr}, as presented in Fig. 4.3.

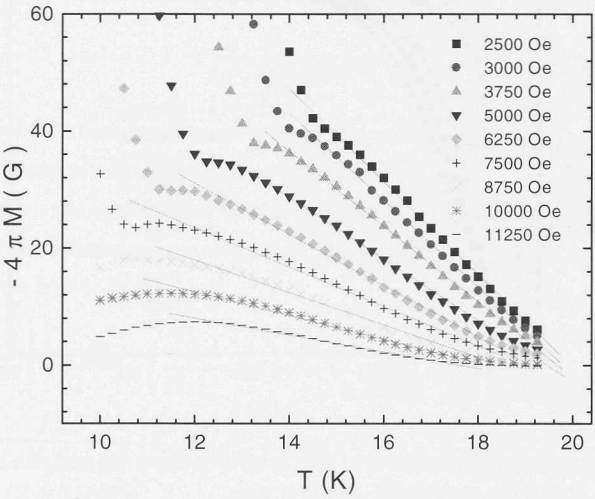

Figure 4.2: *A close-up view of temperature dependent magnetization close to T_c extracted from Fig. 4.1 for various fields. The solid lines are linear fits to the data which will be used for further analysis.*

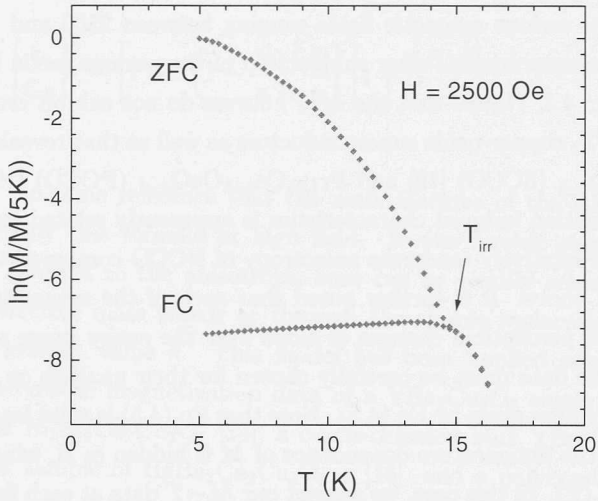

Figure 4.3: *ZFC and FC data in applied magnetic field H=2500 Oe. The arrow indicates irreversibility temperature T_{irr}. The data selected in Fig 4.2. place above the T_{irr}.*

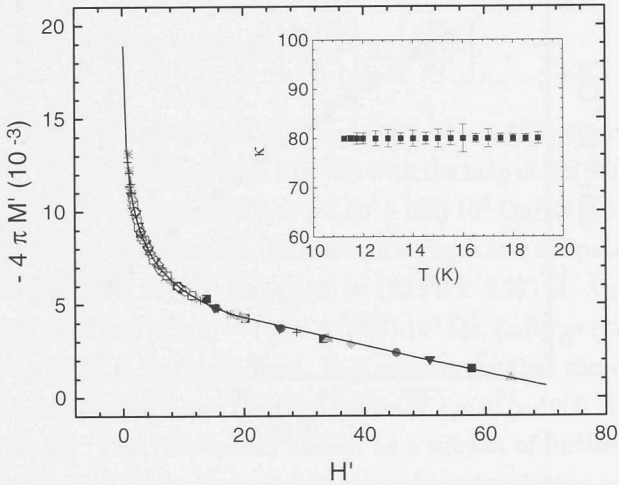

Figure 4.4: *Scaling of magnetization and applied field with respect to* $\sqrt{2}\ H_c(T)$, *with the solid curve representing the Hao-Clem Model fit for* $\bar{\kappa} = 80$ *for the temperature range from 11.25 to 19 K. The error bars on the curve in the inset indicate the standard deviations of the corresponding average values of* $\bar{\kappa}$.

The ensuing analysis of these data follows the method and procedure described in Ref.[4]. According to this method, the magnetic data M and H at each T should be scaled by $\sqrt{2}H_c(T)$ to yield the normalized data $M' = M/\sqrt{2}H_c(T)$ and $H' = H/\sqrt{2}H_c(T)$ (ignoring demagnetization effects) prior to their analysis. To this end, the data at each T in the range considered ($11.25 \leq T \leq 19$ K) were sampled in the form of $-4\pi M_i/H_i$ ratios for i=1,2,..., so that one obtains the required scaled data given by $-4\pi M_i'/H_i' = -4\pi M_i/H_i$. For each of these data corresponding to a certain i, Eq.(4.5), combined with the relation $H_i' = -4\pi M_i' + B_i'$ and an assumed value of $\bar{\kappa}$, will lead to an equation which can be solved for the corresponding B_i'. From the values of B_i' we further computed the corresponding values of M_i' and subsequently the value of H_{ci} for the particular temperature T considered. The value of H_{ci} generally varies over the whole set of data points (i=1,2...). However, a systematic search has been carried out for the determination of a $\bar{\kappa}$ value which produces the set of H_{ci} values with minimum deviation. This procedure is then repeated for each T in the temperature range considered, yielding the corresponding values of M', H', and $\bar{\kappa}$. The result of this analysis is depicted by the $-4\pi M'$ vs H' curve in Fig. 4.4 and the $\bar{\kappa}$ vs T curve in its inset. It is clear that all the calculated $(-4\pi M', H')$ data are nicely represented by the theoretical curve in the entire temperature range mentioned above, in agreement with the result reported in Refs [4, 14, 15, 16, 17].

It is interesting to point out, however, that $\bar{\kappa}$ in the inset remains practically constant over the temperature range considered, in marked contrast to results reported in Refs.[14] and [17] for high-T_c and strongly anisotropic compounds, respectively, where

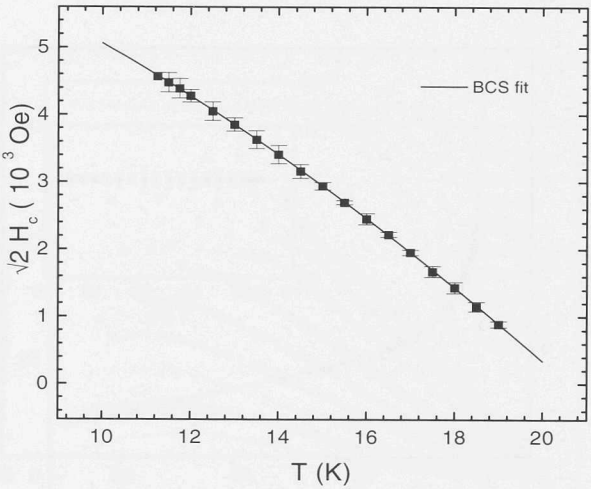

Figure 4.5: *Temperature dependence of $H_c(T)$ obtained from the result of the fitting procedure (full square), The solid curve represents Eq. 4.8 with T_c = 20.6 K. Error bars on the curve indicate the standard deviations from the corresponding average values of $H_c(T)$.*

a drastic departure from mean-field behavior at temperatures close to T_c was observed and attributed to thermal-fluctuation and low dimensionality effects not accounted for by the model proposed in Ref.[4]. Being a low-T_c material and having a relatively moderate anisotropy, our sample appears to be particularly suited for the application of this mean-field model.

The result of the fitting described above gives us both the value of $\bar{\kappa}$ and the temperature -dependent function $H_c(T)$ and hence $H_{c2}(T) = \bar{\kappa}\sqrt{2}H_c(T)$. As a further test of our result, the values computed for H_c at each T are plotted with respect to T in Fig. 4.4 together with the corresponding standard deviations. The theoretical curve deduced from the expansion of the order parameter for $H_c(T)$ is given by [20]

$$\frac{H_c(T)}{H_{co}} = 1.7367\left(1-\frac{T}{T_c}\right)\left[1-0.2730\left(1-\frac{T}{T_c}\right)-0.0949\left(1-\frac{T}{T_c}\right)^2\right], \qquad (4.8)$$

which is also plotted in the same figure, for comparison. An excellent fit of the calculated data with the theoretical curve shown in the figure is obtained for $H_{co} = H_c(0)$ = $(4.80 \pm 0.5)\cdot 10^3$ Oe and $T_c = 20.6 \pm 1.8$ K which practically matches the T_c value of 21 K determined separately by dc low field susceptibility measurement. These near perfect fits in the relatively wide field and temperature ranges in Fig. 4.3 and Fig. 4.4 also attest to the appropriateness of our criterion in the choice of data to be analyzed in addition to the validity of the model adopted for the analysis.

The estimate of the coherence length in the ab plane, ξ_{ab}, at zero temperature can be made, assuming isotropy in the plane, on the basis of the relation, $H_{c2\|c}(0) = \phi_0/2\pi\xi_{ab}^2(0)$, while $H_{c2}(0)$ is determined according to the expression [21]

$$H_{c2}(0) = 0.5758 \left[\frac{\kappa_1(0)}{\kappa}\right] T_c \left[\frac{dH_{c2}}{dT}\right]_{T_c}, \tag{4.9}$$

where $\kappa_1(0)/\kappa = 1.20$ in the dirty limit [22], and $\kappa_1(0)/\kappa = 1.26$ in the clean limit [23]. The slope dH_{c2}/dT can be obtained from Fig. 4.5 with the help of the relation $H_{c2}(T) \simeq \kappa\sqrt{2}H_c(T)$. The value of this slope at T_c is (-4.50 ± 0.5)·10^4 Oe/K. Substituting these values into Eq.(4.9) yields estimates for the coherence length and the penetration depth, namely $H_{c2}(0) = (6.47 \pm 1.27)\cdot 10^5$ Oe, $\xi_{ab}(0) = (22.91 \pm 2.27)$ Å, $\lambda_{ab}(0) = (1651 \pm 181)$ Å in the dirty limit and $H_{c2}(0) = (6.79 \pm 1.33)\cdot 10^5$ Oe, $\xi_{ab}(0) = (22.36 \pm 2.21)$ Å, $\lambda_{ab}(0) = (1788 \pm 178)$ Å in the clean limit. It is noteworthy that the values obtained in this study are considerably larger than the values of $\lambda_{ab}(0) \simeq 1000$ Å determined by other methods [24, 25]. This discrepancy should be a subject of further investigation.

We further conclude that the near perfect theoretical description as demonstrated in our case, in contrast to previous cases involving high-T_c samples, together with the absence of thermal-fluctuation effects as evidenced by the absence of a crossover in our $M - T$ curves, clearly suggests the particular applicability of the Hao-Clem model to low-T_c and moderately anisotropic copper oxide superconductors such as the one studied in this work. It would be interesting to see if the same quality of fitting could be attained from the data on SCCO and PCCO reported in Refs. [18] and [19], where an unexpected high degree of anisotropy is suggested for the sample.

4.3 Vortex State

4.3.1 General properties

In contrast to conventional type-II superconductors, the high-T_c superconductors have a broad resistive transition in applied magnetic field H. The effect of thermal fluctuations has lead to the existence of a vortex liquid originating from a vortex solid. The presence of disorder transforms the vortex lattice into a vortex glass while the vortex liquid remains vortex liquid with some new features due to the pinning effect induced by disorder. Due to the large value of κ and the anisotropy, the melting line is suppressed far below the associated H_{c2} [26] and modifies the $H - T$ phase diagram of the Abrikosov mean-field version. In this phase diagram, the vortex state is determined by competition of several energy scales such as the vortex interaction energy, elastic energy, pinning energy, and thermal energy.

The $Nd_{1.85}Ce_{0.15}CuO_{4-\delta}$ superconductor with relatively low T_c and moderate anisotropy has a relatively insignificant thermal effect. However, the thermal fluctuation in NCCO may still influence the pinning effect on the vortices even when the activa-

tion energy is much bigger than thermal fluctuation, $U \gg T$, as featured by their superconducting resistive transition in magnetic field. At small external current density ($j \ll j_c$) the vortex system shows ohmic behavior with an exponentially small resistance $\rho(T) \sim \rho_0 \exp(-U/T)$ known as thermally-activated-flux-flow (TAFF) [27], which occurs in the high temperature regime. This is different from the behaviors of the BSCCO system and the untwined YBCO single crystals in which TAFF is observed in the low temperature regime which changes over to the free-flux-flow (FFF) as $U \ll T$. Concerning the TAFF mechanism, several models for the activation energy have been proposed in the past. Noteworthy among these are the flux creep model of Yeshurun and Malozemoff [29] and its extension by Tinkham [28] in which they proposed a pinning barrier given by $U \sim 1/H$, and the model of Geshkenbein *et al.* [30] where the vortex system was considered in the plastic state with the plastic barrier $U \sim H^{1/2}$, as well as the so-called 3D vortex liquid by Qiu *et al.*, and a model of quasi-2D vortex liquid with $U \sim \ln H$ [31].

In this study, the thermally-activated-flux-flow is investigated by the Arrhenius plot of the resistivity ($\ln\rho - 1/T$). The measurement was conducted on a single crystal grown by the traveling solvent floating zone method using a four-mirror furnace from the Crystal System Inc. The as-grown crystal was cut into two samples each measuring $\sim$ 1.1x5.2x1.5-mm^3 by size and $\sim$ 56.76 mg by weight (labelled as sample-I) and $\sim$ 1.5x1.5x0.25 mm^3 by size and $\sim$ 3.51 mg by weight (labeled as sample-II). Both as-grown crystals were annealed in flowing N_2 to become a superconductor at $T_c \sim 21$ K with $\Delta T_c < 1$ K. The four contacts on sample I were made by attaching the lead wires with silver paint to the dry silver paint on the sample surface after being annealed in air at 300 ^{0}C for 3 hours, yielding contact resistances of a few ohms per pair. The transport properties were measured with Commercial PPMS Quantum Design with a current of 1 mA. In all of the measurements, the magnetic field was applied parallel to the crystalline c axis in the field range 3000 $\leq H \leq$ 20 000 Oe. Each measurement was started after zero-field cooling (ZFC) to 2 K. Meanwhile, an isothermal magnetization measurement was conducted on sample-II to determine the irreversibility line of the system in order to verify the liquid region. The measurement was carried out using a commercial Quantum Design MPMS-5 magnetometer in the temperature range $5 \leq T \leq 19$ K with the magnetic field applied along the c axis. Each measurement was started after the sample was ZFC to a predetermined temperature. The measurements were carried out with the scan length set of 4 cm.

Figure 4.6 shows the Arrhenius plot of the temperature dependence of ρ_{ab} under different perpendicular fields. It clearly reveals for each field two distinct parts where $\ln\rho$ shows linear dependence upon $1/T$ with different slopes. In each of the Arrhenius plots two characteristic temperatures denoted by T^A and T^B are defined at the upper end of each of the linear segments. The two linear regimes in the Arrhenius plot are similar to those found in multilayer low-T$_c$ superconductors such as Mo/Si [32] , MoGe/Ge

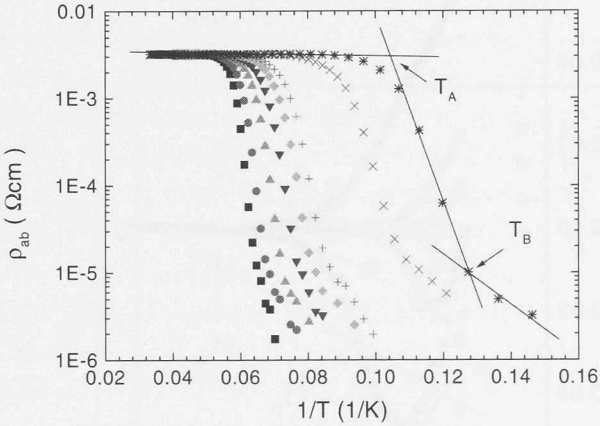

Figure 4.6: *The Arrhenius plot of temperature dependence of ρ_{ab} in various applied fields between 3000 and 20000 Oe parallel to the c axis.*

[33], and NbGe/Ge[34] as well as the high-T_c YBCO thin film [31]. In addition to the Arrhenius plots, Figs 4.7-4.8 show the isothermal magnetic-hysteresis loops $M(H)$ at various temperatures between 5 and 19 K, with the associated penetration field H_p and irreversible field H_{irr}. It is noted that the temperatures T_A and T_B are well above the irreversibility line. This indicates that the Arrhenius plots represent vortex behaviors in the liquid state. These results are summarized in an $H - T$ phase diagram shown in Fig. 4.9.

The linear relationship displayed in the Arrhenius plots indicates the validity of linear temperature dependence of the form $U = U_0(1 - T/T_c)$ for $U(T)$. From the slopes of these plots, the activation energy U_0 at each H is obtained for the two different temperature regimes, and the results are shown in Fig. 4.10, as function of H. The best fit gives $U_0 \sim H^{-\alpha}$ for the low field regimes below 20 kOe with α equal to 0.66 and 0.93 for the high-temperature (High R) and low-temperature (Low R) resistive regime, respectively, although $U_0 \sim \ln H$ also gives a reasonably good fit for both temperature regimes between 20 kOe and 6250 Oe. For $H > 20$ kOe however, the data can only be fitted by the logarithmic law $U_0 \sim \ln H$. Apparently, the crossover from power-law to logarithmic law takes place between 6250 Oe and 20 kOe. The value of α in the low-temperature and low-field regime is close to 1 indicating that the vortex dynamics in this system can be described by the model proposed by Yeshurun and Malozemoff [29]. However the value of α at high temperature and low field differs considerably from the estimated value for vortex dynamics with plastic barrier ($\alpha = 0.5$). The α value of 0.66 in this experiment is on the other hand very close to 0.67 obtained by Graybeal and Beasley [35] in 2D superconducting film of amorphous Mo-Ge. It is also important to note that the high-temperature regime is narrower than the low-temperature one.

A further clarification is needed for the occurrence of the logarithmic law at high

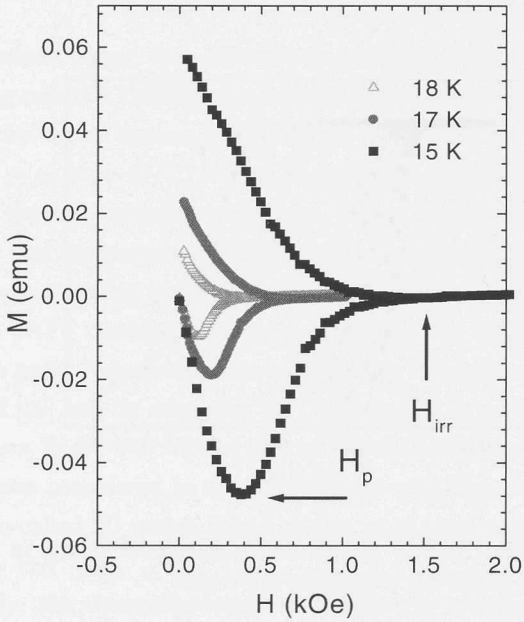

Figure 4.7: *The Isothermal magnetic-hysteresis loops of NCCO single crystal at various temperature between 15 and 18 K.*

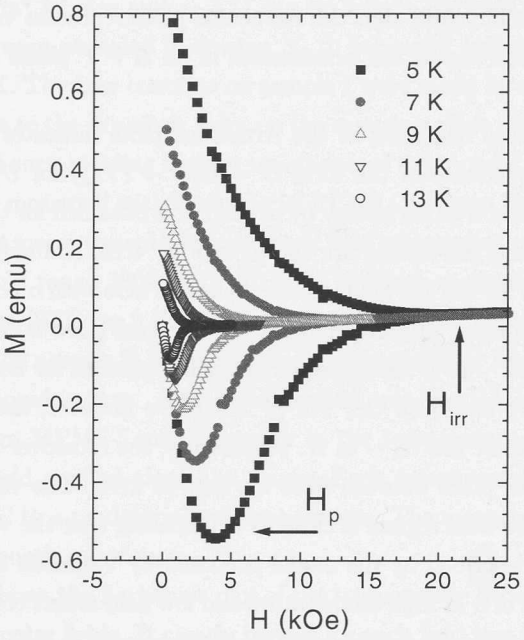

Figure 4.8: *The Isothermal magnetic-hysteresis loops of NCCO single crystal at various temperature between 5 and 13 K.*

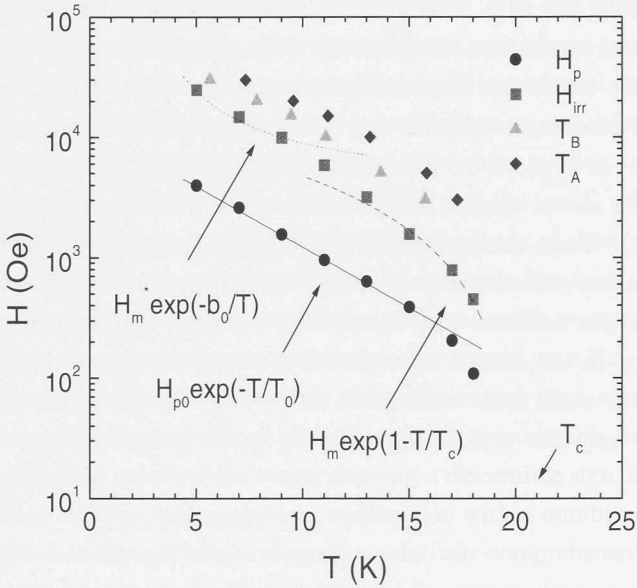

Figure 4.9: *$H-T$ phase diagram for a NCCO single crystal with fits of the temperature dependence of H_p and H_{irr}*

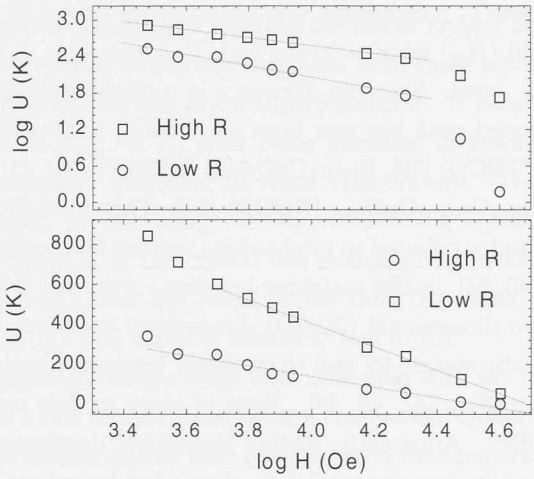

Figure 4.10: *The dependencies of the activation energy on magnetic field for a NCCO single crystal.*

field. This behavior of the flux motion activation energy has been experimentally demonstrated as a feature associated with a quasi-2D vortex state in oxygen deficient YBCO at low field [36, 31]. Theoretically, this field dependent characteristics has also been explained on the basis of thermally activated unbinding of vortex-antivortex pairs taking place above the Berezinskii-Kosterlitz-Thouless (BKT) transition temperature [37]. According to this model, the energy for this to happen is given by $U_0 \sim l_c\phi_0^2/2\pi\mu_0\lambda^2 \ln(\sqrt{\phi_0/B}/\xi)$. In our case, as indicated in the $H-T$ phase diagram of Fig. 4.9 the 2D characteristics is expected to occur instead at the higher field ($\gg H_{2D} \sim 1400$ Oe). Hence the logarithmic law is naturally best fitted for the high field data. This apparent contradiction on the field regimes where the 2D characteristics occurs in the oxygen deficient YBCO and NCCO sample may have its origin in the higher anisotropy in the former case. In other words, the former is basically a 2D system even in the weak field, whereas the latter would become quasi 2D only in the high field. This may also explain the relatively broad crossover region found in this case.

4.3.2 Peak effect

Introduction

The peak effect is now recognized as a general phenomenon in type-II superconductors. It appears as a second peak after the penetration peak in the magnetization curve. In the conventional low-T_c compounds, this phenomenon occurs at high field close to the upper critical-field (H_{c2}) whereas in the high-T_c compounds, it occurs at low field in the magnetization curve. Since its discovery in a single-crystalline $YBa_2Cu_3O_{7-\delta}$ (YBCO) [38], the second peak has now been observed in relatively clean single crystals of $Tl_2Ba_2CuO_6$ (TBCO) [39], $Bi_2Sr_2CaCu_2O_8$ (BSCCO) [40, 41], $La_{2-x}Sr_xCuO_{4-\delta}$ (LSCO) [42] and $Nd_{1.85}Ce_{0.15}$ $CuO_{4-\delta}$ (NCCO) [24]. This anomalous effect has been extensively studied, and attributed to mechanisms varying from collective pinning [43], surface barriers [39, 40, 24], lattice matching between vortex and defect structure [44], three dimensional-two dimensional (3D-2D) dimensional crossover [45], crossover between elastic and plastic states [46] and to crossover between quasilattice vortex glass and disordered vortex glass [47, 48, 49]. None of these models provides a complete description of the effect. Apparently, further theoretical development requires more complete and high-quality experimental data than what have been available to date. For instance, the fact that most of the available data are obtained by bulk measurements of the magnetization loop, may somehow suppress the salient feature of a sharp transition in the peak effect. Furthermore, while generally reported with a clear on-

set temperature below T_c, most of the data fail to delineate the temperature range in which this remarkable effect persists. An exception to this has been reported on BSCCO [50, 51] for which a temperature range of 22 to 28 K was cited for the observation of the peak effect. Added to these shortcomings are the non-uniform quality of samples studied so far. As a consequence, additional experimental data and related phenomenological analysis are needed before a comprehensive and definitive picture of the associated vortex phase diagram may emerge from these studies.

The relatively moderate anisotropy ($\gamma = 200$) [52] and the low T_c value (T_c between 21 and 24 K) of NCCO offer a special advantage for the study of those putative transitional effects, as the phenomena are expected to be relatively free from thermal complications and to be within an easily accessible range for magnetic measurements. In this section, the result of magnetic-hysteresis loop measurements on a $Nd_{1.85}Ce_{0.15}CuO_{4-\delta}$ single crystal are reported which definitely show the second peak effect. In contrast to the results reported by Andrade *et al.* [53], a clearly reproducible peak effect is observed within a limited temperature range, showing a discernible sign of disappearance of the arrow head at lower temperature in conjunction with a number of other effects. Analysis of these coincidental effects suggests a relatively comprehensive picture of the vortex states covering the peak-effect region and its surrounding area in the $H - T$ phase diagram.

Experiments

The experiments were performed on a single crystal of $Nd_{1.85}Ce_{0.15}CuO_{4-\delta}$ grown by the travelling solvent floating zone (TSFZ) method using a four-mirror furnace from Crystal System Inc. The crystal with dimensions of $\sim$ 1.5 x 2.5 x 0.01 mm^3 and mass of 1.6 mg was obtained by cleaving the as-cut crystal along the ab plane in air. The crystal has typically different dimensions from those reported in the previous section. The as-grown crystal was not a superconductor. It became superconducting below T_c $\sim$21 K (with ΔT_c $\sim$1 K) after being annealed in flowing N_2 gas at 900 ^{0}C for 30 h and subsequently quenched to room temperature. The superconductivity can be easily removed by annealing the superconducting crystal at 900 ^{0}C in air. The elemental composition of the crystal was examined by means of Electron Micro Probe Analysis (EPMA), and the result shows that the molar ratios are given by Nd:Ce:Cu:O=1.98:0.15:1:3.59 which is relatively rich in Nd.

Isothermal magnetic-hysteresis loops were measured with the magnetic field H applied parallel to the c axis of the crystal using a commercial Quantum Design MPMS-5 magnetometer. The measurements were carried out in the temperature range $5 \leq T \leq 20$ K, with field steps of $10 \leq H \leq 50$ Oe and $50 \leq H \leq 350$ Oe below and above the second peak, respectively. Each measurement was started after the sample was ZFC to a predetermined temperature with the scan length set at 4 cm.

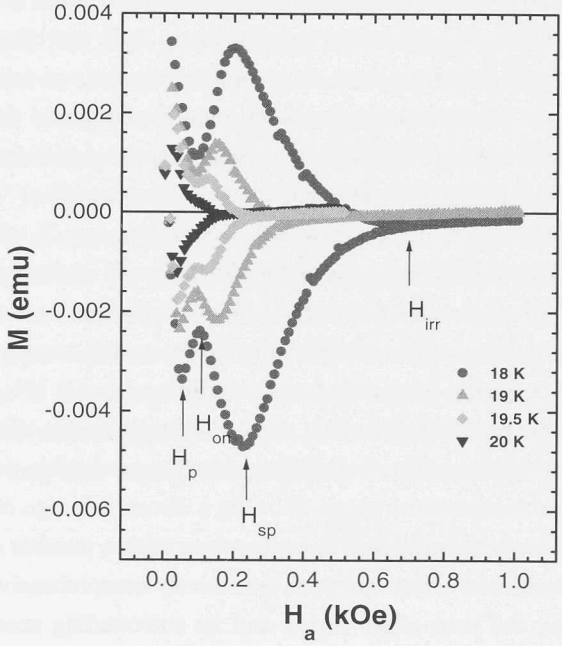

Figure 4.11: *Isothermal magnetic-hysteresis loops of a NCCO single crystal at various temperatures between 18 and 20 K.*

Results and discussion

Figs. 4.11 - 4.13 show the magnetic-hysteresis loops $M(H)$ in the low-field region with the penetration field H_p, onset field for the second peak H_{on}, the second peak H_{sp}, and the irreversible field H_{irr} indicated on the curves. The curves exhibit the following features : (1) An onset temperature of the second peak at T ~19.5 K, which is very close to T_c, with H_{on} ~100 Oe, in reasonable agreement with an observation reported previously [53, 54]. (2) A discernible disappearance of the second peak below about T ~10 K (T/T_c <0.5), in clear contrast to results reported in Refs. [53] and [54]. (3) An abrupt increase of the penetration field at about 10 K, where the second peak disappears. It must be stressed that in all high T_c cases reported so far, the onset temperature of the peak effect generally lies far below T_c (T/T_c <0.5). Furthermore, the disappearance of the effect was not commonly reported, except in the case of a BSCCO crystal for which a temperature range between 22 and 28 K was cited for the observation of the effect [50, 51].

Following the scaling treatment introduced previously for a BSCCO crystal [55], the $M(H)$ curves at various temperatures presented in Figs. 4.11-4.13 are similarly treated here. For each curve, the field and moment are scaled with the magnetic moment (m^*) and the magnetic field (h^*) at the first penetration point indicated in the

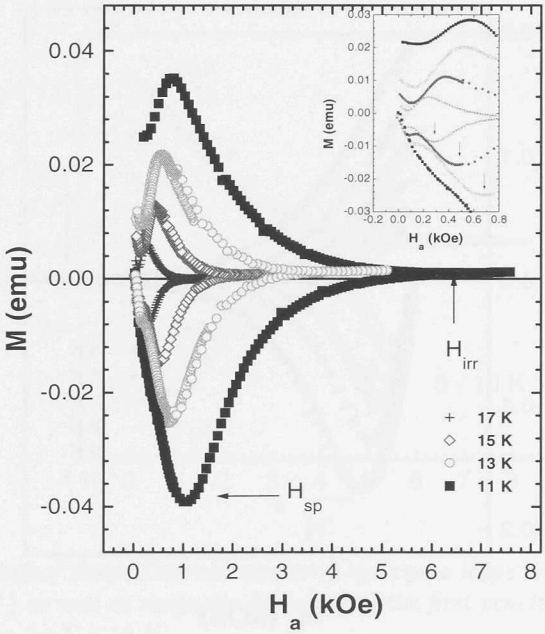

Figure 4.12: *Isothermal magnetic-hysteresis loops of a NCCO single crystal at various temperatures between 11 and 17 K.*

figure. The results are presented separately in Fig. 4.14 and Fig. 4.15 for different temperature ranges. Figure 4.14 shows the normalized magnetization curves at temperatures between 5 and 10 K, which are below the temperature range of the second peak. A remarkable scaling behavior is displayed over the entire range of the hysteresis loop for 5,6 and 7 K. It is further observed that a distinct deviation from the scaling behavior begins to show up at 9 K which is around the lower end of the temperature range of the second peak. In this temperature range the scaling characteristics is almost completely lost; it is retained only in the very narrow region far below h^* as depicted in Fig. 4.15. Unfortunately, it is impossible to investigate the expected recovery of the scaling behavior at the high-temperature end of the peak-effect (T ~19.5 K), as the interval between this temperature and the critical-transition temperature is simply too narrow to allow a meaningful comparison of distinctly different magnetization curves.

Another important aspect revealed by Figs. 4.14 and 4.15 is the onset and disappearance in the different temperature regions, of the symmetry between the two branches of the hysteresis loop. It is apparent that a pronounced asymmetry features in the scaled data at temperatures below 10 K. To a lesser extent, a similar feature is also perceptible for the data at 20 K represented by the innermost curve in Fig. 4.15. On the other hand, a symmetrical shape of the hysteresis loops is consistently displayed in the figure for all curves with T lying within the temperature range of the peak effect.

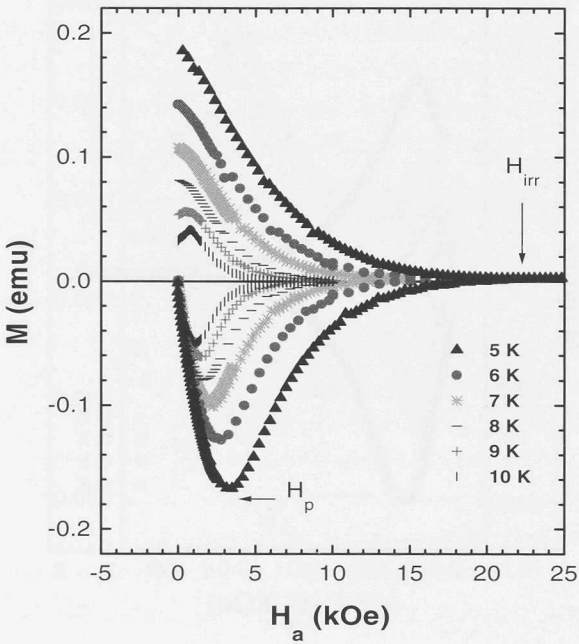

Figure 4.13: *Isothermal magnetic-hysteresis loops of a NCCO single crystal at various temperatures between 5 and 10 K.*

Similar behavior has previously been reported for a BSCCO [50, 51]. It is important at this point to recall that the symmetrical shape of the hysteresis loop is supposed to indicate a dominant role of the bulk pinning mechanism, while the decrease of the symmetry is understood to signify the increasing role of the surface or the geometrical barriers in the pinning mechanism [51]. Hence, it is natural to suggest on this general ground that the second-peak effect is expected to appear in a temperature and field regime where the bulk pinning effect is dominant and to disappear outside this regime due to suppression of the pinning mechanism. This general picture appears to be well in line with the suggestion offered in Ref. [55]. A more detailed description will emerge in the following discussion.

For the purpose of further analysis, the experimental $M - H$ curves in Figs. 4.11-4.13 are converted to $H - T$ semilog plots in Fig. 4.16. This conversion is carried out by taking for each temperature T, the values of H_p at the first minimum, H_{on} at the first maximum, H_{sp} at the second minimum of the associated magnetization curves in Figs. 4.11-4.13 which are then transferred to the corresponding points in Fig. 4.16. The data points for H_{irr} in the same figure are obtained, again for each T, from the corresponding points of splitting between the lower and upper branches of the $M - H$ curves in Figs. 4.11 - 4.13. This transformation of data allows a better description and a more convenient study of the temperature and field dependent behaviors of the

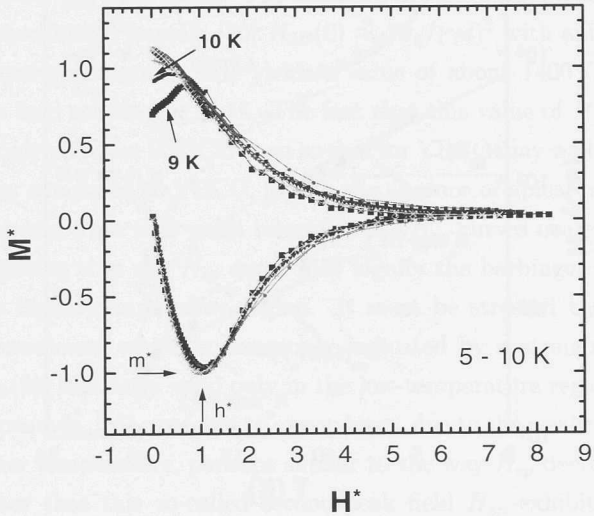

Figure 4.14: *Scaling of the isothermal magnetic-hysteresis loops with respect to magnetic moment (m^*) as well as magnetic field (h^*) at the first penetration point for low temperature regime 5< T <10 K.*

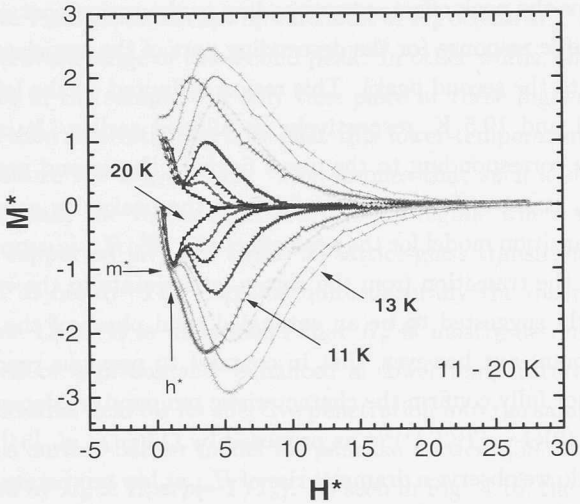

Figure 4.15: *Scaling of the isothermal magnetic-hysteresis loops with respect to magnetic moment (m^*) as well as magnetic field (h^*) at the first penetration point for low temperature regime 11< T <20 K.*

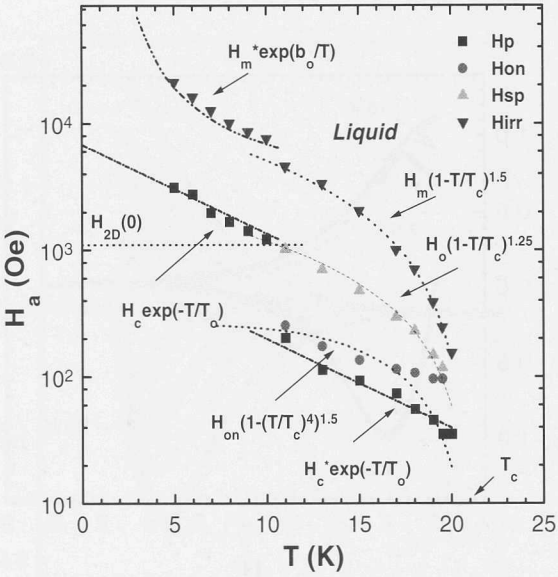

Figure 4.16: *$H-T$ phase diagram for a NCCO single crystal with fits of the temperature dependence of H_p, H_{on}, H_{sp} and H_{irr}. See text for the discussion.*

sample on the basis of available theoretical models, and thus paving the way for the construction of the associated phase diagram.

In Fig. 4.16, the data are presented together with the theoretical fits. One of the noticeable features in the $H-T$ diagram is the appearance of an apparently well-confined region for the peak effect, corresponding to the region containing the "rising" part of the magnetic response (or the descending part of the associated magnetization curve pertaining to the second peak). This region is limited on the left hand and right hand sides by 11 and 19.5 K, respectively, as alluded earlier. It is bounded below by the H_{on} curve corresponding to the onset fields of the second peak, and bounded above by the H_{sp} curve representing the fields at the peaks. In accordance with the order-disorder transition model for the peak effect [47, 48], H_{on} is supposed to represent the boundary for the transition from the vortex-lattice state to the vortex-glass state, which was recently suggested to be an entangled solid phase of the vortices [49]. It is important to point out however, that in contrast to previous reports [53, 54], our data for H_{on} do not fully confirm the characteristic temperature dependency expressed by $H_{on}(T) = H_{on}(0)(1-(T/T_c)^4)^{3/2}$ as proposed by Giller *et al.* [54], particularly for $T/T_c > 0.8$. Nor do we observe a dramatic rise of H_{on} at low temperature as reported by Andrade *et al.* [53]. The upper boundary H_{sp} marks the turning point corresponding to the sharp reversal of the magnetic response of the sample, which is presumably a consequence of a sudden weakening of the pinning strength. One potential mechanism responsible for this change of pinning strength at relatively high magnetic fields is

a dimensional crossover from a 3D to a 2D vortex state. This 2D vortex state may exist below the vortex melting line $H_{irr}(T)$ as a result of the pancake-vortex layer decoupling at relatively high fields. An estimate of the dimensional crossover field based on the approximate formula [56] $H_{2D}(0) \approx 4\Phi_o/(\gamma d)^2$ with anisotropy [52] $\gamma = 200$, and interlayer spacing $d = 12\mathring{A}$ yields a value of about 1400 Oe for $H_{2D}(0)$ as indicated on the field axis in Fig. 4.15. The fact that this value of $H_{2D}(0)$ is closer to the value commonly cited for BSCCO than to that for YBCO may well be related to the higher anisotropy compared to YBCO, due to the absence of apical oxygen in NCCO. A straight line drawn from that point intersects the H_{sp} curves near its upper end, at $T \sim 11$ K, suggesting that our H_{sp} curve may signify the harbinger of a dimensional crossover in the higher-temperature region. It must be stressed that the boundary of dimensional crossover, which is commonly indicated by a straight horizontal line drawn from $H_{2D}(0)$, is strictly valid only in the low-temperature region far away from T_c. On general grounds, it is expected to curve down, due to the weakening of interlayer coupling at higher temperature, perhaps similar to the way H_{sp} decreases towards T_c. One notes further that this so-called second-peak field H_{sp} exhibits a temperature dependence described very closely by $H_{sp}(T) = H_o(1 - T/T_c)^{1.25}$, with $H_o = 2650$ Oe, resembling the high-temperature part of H_{irr} to be discussed below. Unfortunately this interesting observation has so far remained unexplained.

It is important to note at this point that the H_{on} curve in Fig. 4.16 is located slightly above the penetration field curve H_p, supporting our view that the peak effect occurs in a state where an effective penetration of the external field as well as the formation of a quasilattice structure have taken place in the sample, by which the pinning mechanism becomes operative. Further, an abrupt upward shift of H_p occurs at T around the lower limit of the temperature range of the second peak. In other words, effective formation of the vortex state in the sample will only take place at these higher magnetic fields below 10 K. It is then interesting to note that this lower-temperature part of the H_p curve is located above the $H_{2D}(0)$ line. This implies that such a strong increase in magnetic field will take the vortex right into the 2D regime where no vortex lattice structure can be supported [57] and hence no lattice-glass transition or second-peak effect is expected to occur. This explains quite naturally the disappearance of the second peak below 11 K. It is understood that H_p is mostly determined by barrier effects, and this effect is presumably enhanced at lower temperature, explaining the need of a higher external field for its effective penetration into the sample. Ignoring the relaxation effect, a surface-barrier model for pancake vortices [58] has been proposed to be characterized by $H_p \simeq H_c exp(-T/T_o)$. As seen in Fig. 4.16, the low-temperature part of H_p fits very well with the data for $H_c = 6800$ Oe and $T_o = 6.2$ K. On the other hand, the higher-temperature part of H_p fits only partially with the theoretical curve (using $H_c^* = 1000$ Oe), exhibiting a distinct deviation at temperatures close to T_c. A vortex-line model with its prediction of $H_p \sim (T_c - T)^{3/2}/T$ does not work either for

this part of the data. We suspect that an additional effect of geometrical barriers may play a greater role at higher temperature [60, 61].

Turning our attention to the irreversibility line in Fig. 4.16, we note immediately that the data are clearly divided into two parts. The high-temperature part (11 K $< T <$ 19.5 K) displays an excellent fit to the theoretical curve given by $H_{irr} = H_m(1 - T/T_c)^{1.5}$ with $H_m = 13500$ Oe, which was supposed to be a consequence of depinning of the vortices or the combined effect of thermal and quantum fluctuations [62]. We note once again that Andrade *et al.* [53] have reported a fit of their data with basically the same form with $H_m = 23000$ Oe and an exponent of 2.4. One further observes that below 10 K, the irreversible line is better characterized by an exponential law, $H_{irr} = H_m^* exp(b_o/T)$ where $H_m^* = 2500$ Oe and $b_o = 10$ K. This behavior has been suggested in the Josephson-coupled layer-superconductor model with moderate anisotropy [63]. A similar change of the temperature-dependent behavior of H_{irr} was also observed in a single crystal of BSCCO [63, 41, 64, 65, 66] and TBCO [67]. In contrast to that observation however, the discontinuity found here involves the value of H_{irr} instead of merely its slope. Furthermore, a change in sign of the slope was observed at the onset temperature in the case of the BSCCO and TBCO systems. In our case, this change can not be observed since the onset temperature at the higher end is too close to T_c to allow such a detailed analysis. It is conceivable to expect however, that some change in H_{irr} should occur at both ends of the temperature range of the peak effect. In our case for instance, the discontinuity at lower temperature and higher magnetic field could perhaps be attributed to some change in the interlayer-coupling mechanism, while the change at temperatures close to T_c may well be due to fluctuation-induced depinning effects. It is nevertheless too early at this stage to pin down on the exact nature of the changes. In fact, the theoretical model mentioned above was formulated for a 3D-like vortex fluctuation at $H \ll H_{2D}(0)$, which is not exactly the condition met in our experiment. But the fact that it occurs concurrently with the onset or disappearance of the peak effect should provide an important clue for unraveling its underlying mechanism.

Finally, a note of comparison with the vortex-phase-transition picture proposed recently by Giller *et al.* [54] will be in order. We note in the first place that their $H-T$ diagram does not indicate the existence of a low-temperature limit for the entangled solid phase as revealed by our experimental data and indicated in the vortex phase diagram. We should also point out that in our proposed phase diagram, a "buffer" vortex phase of 2D or quasi-2D character appears between the phase boundary of the entangled solid and the vortex melting line $H_{irr}(T)$. In addition to this, detailed temperature-dependent behavior of the various "phase" boundaries obtained from our data is also at variance with theirs.

Conclusion

We have presented magnetization data on a NCCO single crystal at various temperatures, which show for the first time in this system a clear temperature delineation on both ends for the second-peak effect and an abrupt increase of the penetration field at its lower end. Analysis of the data on the basis of some of the existing models has led to a suggested vortex-state phase diagram for the sample. It also confirms the crucial role of pinning with weak disorder in the peak effect, and suggests the necessary condition of effective penetration by the external field along with the formation of a quasilattice vortex state which is only possible in the 3D vortex regime. Lacking any of these factors will simply lead to an unfavorable condition for the appearance of the peak effect. We have further found a compelling reason to include a quasi-2D vortex regime in our $H-T$ diagram in order to understand the important characteristics of our data. Our $H-T$ phase diagram also reveals a number of features in conjunction with the appearance of this anomalous effect which requires a more comprehensive and coherent explanation. Finally, it is important to point out that our data do not agree very well with those obtained by the other groups on the same basic system, prepared however by different processes.

4.3.3 Relaxation in the peak effect regime

Introduction

The phenomenon of magnetic relaxation arising from thermally activated flux creep has been most intensively studied in high temperature superconductors since its first observation in YBCO [29]. Aside from the effect of temperature enhancement, the so called 'giant flux creep' in this new class of cuprate oxide superconductors is also known to work on a novel pinning mechanism different from the model formulated by Anderson and Kim [68]. It has recently been shown that a similar effect is observed in the lower temperature species including LSCO [69] and NCCO [70]. We report here the result of magnetic relaxation measurement on a high quality NCCO single crystal in connection with the temperature variation of the second peak effect reported previously [5]. Further analysis on the pinning barrier will also be conducted on the basis of the collective flux creep model [71].

Experiments

Our sample was a single crystal of $Nd_{1.85}Ce_{0.15}CuO_{4-\delta}$ grown in a four-mirror furnace of Crystal System Inc. as described in Chapter 2. The magnetization measurements

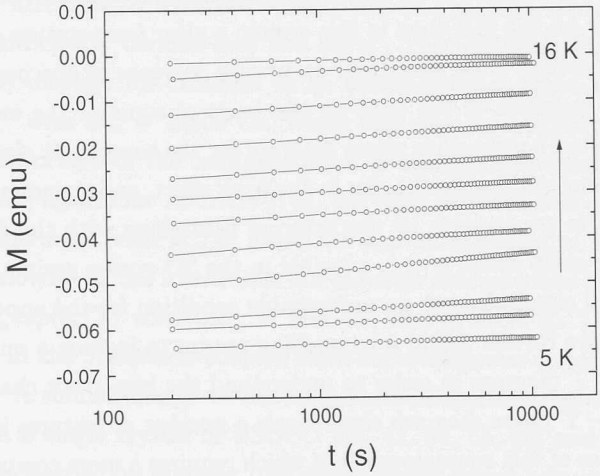

Figure 4.17: *Time dependence of magnetization in the FS mode at various temperature between 5 and 17 K at 750 Oe. The lines are guides to the eyes.*

were performed in a magnetic field, H, applied along c axis in a Quantum Design SQUID magnetometer with a scan length of 4 cm, and over a temperature range of 5 $\leq T \leq$ 17 K. For the measurement of relaxation data, the sample was first zero field cooled (ZFC) to 5 K, and then heated to a desired measuring temperature within the temperature range mentioned above. The magnetic field was then ramped up from 0 to 750 Oe and kept fixed during the measurement, this will later be called the forward-sweep (FS). As reverse-sweep (RS), the applied field is initially raised up to 25 kOe in order to ensure full penetration of the flux into the sample at the measurement temperature, then lowered to 750 Oe prior to measurement. The applied field strength was chosen to probe the second peak region in the $H - T$ phase diagram described in the previous section [5]. The time window for data sampling is 200 s and the entire time span of each measurement is about 3 hours. The data are shown in Figs. 4.17 and 4.18.

Results and discussion

The data of the remanent magnetization $M(t)$ were measured isothermally as function of the time t at various temperatures. We note that the remanent magnetization in the higher temperature regime decays at progressively faster rates as evidenced by its increasing deviation from the linear dependence on $ln(t)$. This is illustrated by the temperature dependence of the relaxation rate $S = -dln(M)/dln(t)$ obtained from forward-sweep and reverse-sweep measurements as plotted in Fig. 4.19. We observe further from the figure that the two curves exhibit qualitative similarity for $T \leq 15$

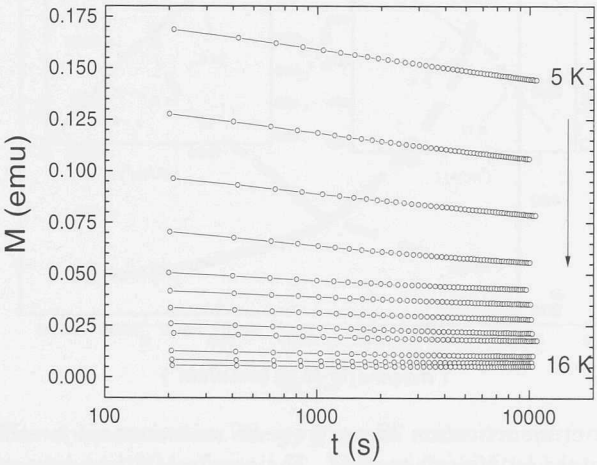

Figure 4.18: *Time dependence of magnetization in the RS mode at various temperature between 5 and 16 K at 750 Oe. The lines are guides to the eyes.*

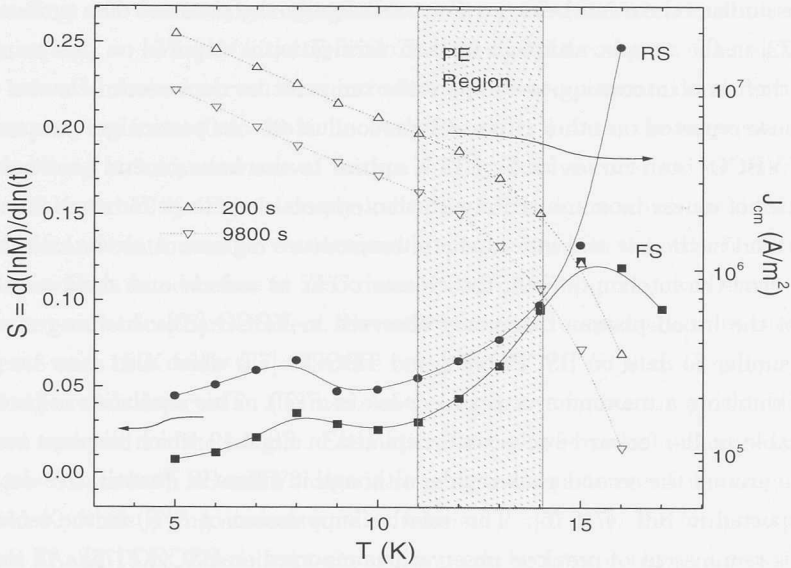

Figure 4.19: *Temperature dependence of magnetization relaxation rate $S(T)$ and the critical current density $j_{cm}(T)$ from FS and RS measurements. The lines are guides to the eyes.*

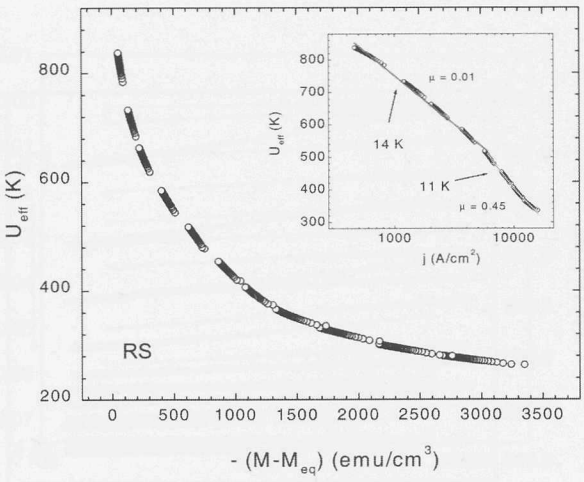

Figure 4.20: *Flux creep activation energy from RS measurement for temperatures from 5 to 16 K determined by Maley's method. The results of fitting between 8 to 15 K are indicated in the inset.*

K, and even coincide at T= 14 K. Beyond 15 K, their variations with respect to T are marked by distinctly different characteristics. This means that apart from the small temperature range in the vicinity of $T \sim 14$ K, the relaxation processes in the reverse-sweep and forward-sweep cases generally proceed in an asymmetric manner. This dissimilar relaxation behavior may well signify the presence of a surface barrier effect [72] in the sample, although further clarification is required on this point.

Further, it is interesting to compare the temperature dependent behavior of $S(T)$ with those reported on other cuprate superconductors. In particular, compared with that of YBCO, both curves for $T \leq 15$ K appear to share the general qualitative characteristics of a near monotonic rise with the temperature except for some interruption of the trend in the low and intermediate temperature regions. A closer look, however, reveals that the interruptions in these cases occur as narrow and shallow valleys instead of the broad plateau commonly observed in YBCO [73]. In this respect, it is rather similar to data on BSCCO [74] and TBCCO [75] which also show no plateau, while exhibiting a maximum or double peak in $S(T)$. This similarity is particularly remarkable in the forward-sweep data depicted in Fig.4.19 which displays two broad maxima around the second peak region, although it differs in quantitative detail from that reported in Ref. [74, 75]. This relative suppression of $S(T)$ in the second peak region is reminiscent of previous observations reported on BSCCO [76]. All these particular behaviors are supposed to be the outcome of an intricate interplay between the pinning mechanism and the thermal effect, with further complication from the surface or geometrical barrier effect.

In order to compare the data with some of the existing models, the method of

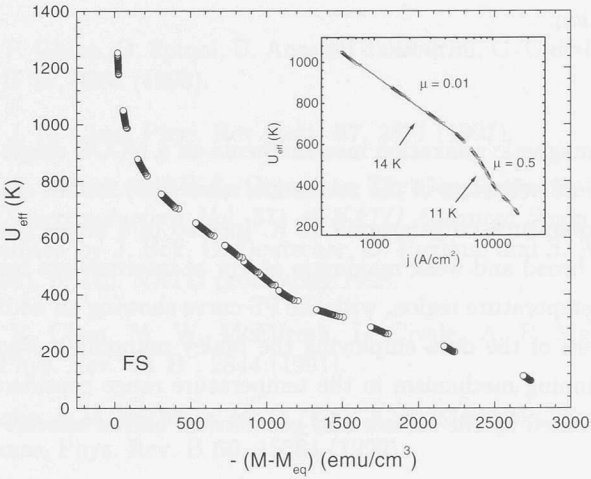

Figure 4.21: *Flux creep activation energy from FS measurement for temperatures from 5 to 17 K determined by Maley's method. The results of fitting between 8 to 16 K are indicated in the inset.*

Maley *et al.* [77] is applied for determination of the flux creep activation energy as a function of magnetization or screening current density. The results for reverse-sweep and forward-sweep data are shown respectively in Fig.4.20 and 4.21 as the set of U_{eff} vs - $(M - M_{eq})$ segments for various temperatures, with M_{eq} is the associated average of ascending and descending magnetization. Here, the effective activation energy is written as $U_{eff} = -T\ln|dM/dt| + T_0$ with T_0 is an additive constant. The segments are scaled into a "universal curve" after introduction of a temperature dependent additive constant varying from 40 to 60 K. In both RS and FS data, the segments can only be scaled onto a "universal curve" with a single additive constant for temperatures between 8 K and 12 K. This is clearly indicated in the figure which are different from the smooth and continuous curves obtained in many cases. On the other hand, a similar feature has been noted before in ZFC data of BSCCO [76], and it was attributed to a surface or geometrical barrier effect. Nevertheless, an attempt made to fit these curves between 8 and 15 K with the collective creep model [71] $U(j) \simeq U_c/\mu((j_c/j)^\mu - 1)$, leads to the result depicted in the insets of the respective figures for which a disc shape has been assumed for the sample. Estimation from the fit yields a glassy exponent of about $\mu = 0.5$ for both RS and FS data in roughly the same temperature range between 8 and 11 K, while giving a much smaller value of $\mu = 0.01$ in the temperature range between 11 and 15 K. This abrupt change of μ can be interpreted as a crossover from a "rigid" to a "soft" vortex glass as we move from the lower to the higher temperature regimes of the peak effect. The change of μ in the peak effect regime has also been reported by Giller *et al.* [54] although it differs in quantitative details from our result. Admittedly, in view of the possible complication from surface or geometrical barrier

effect as reflected by the "imperfection" of our Maley plots, this analysis is subject to further clarification.

Conclusion

The result of magnetic relaxation measurements on a NCCO single crystal has indicated asymmetrical behaviors of the relaxation rates $S(T)$ for RS and FS data except in a narrow temperature range around 14 K. Instead of a broad plateau, both $S(T)$ curves display a broad and weak maximum at low or intermediate temperature before the peak effect temperature region, with the FS curve showing an additional maximum at 16 K . Analysis of the data employing the Maley mapping method has suggested a crossover of pinning mechanism in the temperature range considered, although the picture is complicated by the surface and geometrical barrier effects.

References

[1] M. Scavini, P. Ghina, G. Spinol, U. Anselmi Tamburini, G. Chiodelli, and G. Flor, Phys. Rev. B **58**, 9385 (1998).

[2] Z. Hao and J. R. Clem, Phys. Rev. Lett. **67**, 2371 (1991).

[3] P. Fournier, E. Maiser, and R. L. Greene, in *The Gap Symmetry and Fluctuations in High-T_c Superconductors*, Vol. 371 of *NATO Advanced Study Institute, Series B: Physics* edited by J. Bok, G. Deutscher, D. Pavuna, and S. A. Wolf (Plenum, London, 1998), p. 145. NATO proceeding 1998.

[4] Z. Hao, J. R. Clem, M. W. McElfresh, L. Civale, A. P. Malozemoff and F. Holtzberg, Phys. Rev. **43 B** , 2844 (1991).

[5] A. A. Nugroho, I. M. Sutjahja, M. O. Tjia, A. A. Menovsky, F. R. de Boer, and J. J. M. Franse, Phys. Rev. B **60**, 15384 (1999).

[6] A. A. Nugroho, I. M. Sutjahja, A. Rusydi, M. O. Tjia, A. A. Menovsky, F. R. de Boer, and J. J. M. Franse, Phys. Rev. B **60**, 15379 (1999).

[7] A. A. Nugroho, I. M. Sutjahja, M. O. Tjia, A. A. Menovsky, F. R. de Boer, and J. J. M. Franse, Physica C **332**, 374 (2000).

[8] A. A. Abrikosov, Zh. Eksp. Teor. Fiz. **32**, 1442 (1957).

[9] A. L. Fetter and P. C. Hohenberg, in *Superconductivity* , edited by R. D. Parks (Marcel Dekker, New York, 1965), Vol 1, pp. 138-167.

[10] V. G. Kogan, M. M. Fang and S. Mitra, Phys. Rev. B **38**, 11958 (1988).

[11] S. Mitra, J. H. Cho, W. C. Lee, D. C. Johnston and V. G. Kogan , Phys. Rev. B **40**, 2674 (1989).

[12] J. R. Thompson, D. K. Christen, H. A. Deeds, Y. c. Kim, J. Brynestad, S. T. Sekula and J. Budai, Phys. Rev. B **41**, 7293 (1990).

[13] M. Tuominen, A. M. Goldman, Y. Z. Chang and P. Z. Jiang, Phys. Rev. B **42**, 412 (1990).

[14] Qiang Li, M. Suenaga, Junho Gohng, D. K. Finnemore, T. Hikata and K. Sato Phys. Rev. **46**, 3195 (1992).

[15] Junghyun Sok, Ming Xu, Wei Chen, B. J. Suh, J. Gohng, D. K. Finnemore, M. J. Kramer, L. A. Schwatzkopf and B. Dabrowski, Phys. Rev. **51**, 6035 (1995).

[16] Mun-Soeg Kim, Myoung-Kwang Bae, W. C. Lee and Sung-Ik Lee, Phys. Rev. **51**, 3261 (1995).

[17] Yi Zhuo, Jae-Hyuk Choi, Mun-Seog Kim, Wan-Seon Kim, Z. S. Lim, Sung-Ik Lee and Sergey Lee, Phys. Rev. **55**, 12719 (1997).

[18] L. Fábrega, M. A. Crusellas, J. Fontcuberta, X. Obradors, U. Welp and G. W. Crabtree, Physica C **194 - 196**, 2253 (1994).

[19] L. Fábrega, J. Fontcuberta, S. Pinol, X. Obradors, U. Welp and G. W. Crabtree, Europhys. Lett **24**, 595 (1993).

[20] J. R. Clem, Ann. Phys. (NY) **40**, 268 (1966).

[21] B. Mühlschlegel, Z. Phys. **155**, 584 (1967).

[22] N. R. Werthamer, E. Helfand and P. C. Hohenberg, Phys. Rev. **147**, 295 (1966).

[23] Eilenberger, Phys. Rev. **153**, 584 (1967).

[24] F. Zuo, S. Khizroev, Xiuguang Jiang, J. L. Peng and R. L. Greene, Phys. Rev. **49**, 12326 (1994).

[25] N. C. Yeh, U. Kriplani, W. Jiang, D. S. Reed, D. M. Strayer, J. B. Barner, B. D. Hunt, M. C. Foote, R. P. Vasques, A. Gupta, A. Kussmaul, Phys. Rev. **48**, 9861 (1993).

[26] A. Houghton, R. A. Pelcovits, and A. Subdo, Phys. Rev. B **40**, 6763 (1989).

[27] P. H. Kes, J. Aarts, J van den Berg, C. J. van der Beek and J. A. Mydosh, Superc. Sc. Technol. **1**, 242 (1989).

[28] M. Tinhkam, Phys. Rev. Lett. **61**, 1658 (1988).

[29] Y. Yeshurun and A. P. Malozemoff, Phys. Rev. Lett. **60**, 2202 (1988).

[30] V. B. Geshkenbein, M. V. Fiegel'man, and V. M. Vinokur, Physica C **162-164**, 2511 (1991).

[31] X. G. Qiu, B. Wuyts, M. Maenhoudt, V. V. Moshchalkov, and Y. Bruynseraede, Phys. Rev. B **52**, 559 (1995).

[32] N. Y. Fogel, Victoria G. Cherkasova, Olga A. Koretzkaya, Anatoly S. Sidorenko, Phys. Rev. B **55**, 85 (1997).

[33] W. R. White, A. Kapiltunik, and M. R. Beasley, Phys. Rev. Lett. **66**, 2826 (1991).

[34] X. G. Qiu, B. R. Zhao, S. Q. Guo, J. R. Zhang, L. Li, F. Ichikawa, T. Nishizaki, T. Fukami, Y. Horie, and T. Aomine, Phys. Rev. B **47**, 14 519 (1993).

[35] J. M. Graybeal and M. R. Beasley, Phys. Rev. Lett. **56**, 173 (1986).

[36] Yu. Eltsev, W. Holm, and Ö Rapp, Phys. Rev. B **49**, 12 333 (1994).

[37] H. J. Jensen, P. Minnhagen, E. Sonin, and H. Weber, Europhys. Lett. **20**, 463 (1992).

[38] M. Daeumling, J. M. Seuntjen, and D. C. Larbalestier, Nature **346**, 332 (1990).

[39] V. N. Kopylov, A. E. Koshelev, I. F. Schegolev and T. G. Togonidze, Physica C **170**,291 (1990)

[40] N. Chikumoto, M. Konczykowski, N. Motohira, and A. P. Malozemoff, Phys. Rev. Lett **69**, 1260 (1992)

[41] K. Kadowaki and T. Mochiku, Physica C **195**, 247 (1992)

[42] T. Kimura, K. Kishio, T. Kobayashi, Y. Nakamura, N. Motohira, K. Kitazawa, and K. Yamafuji, Physica C **192**, 247 (1992).

[43] L. Krusin-Elbaum, L. Civale, V. M. Vinokur, and F. Holtzberg, Phys. Rev. Lett **69**, 2280 (1992)

[44] G. Yang, P. Shang, S. D. Sutton, I. P. Jones, J. S. Abell and C. E. Gough, Phys. Rev. B **48**, 4054 (1993)

[45] T. Tamegai, Y. Iye, I. Ogura, K. Kishio, Physica C **213**, 33 (1993)

[46] Y. Abulafia, A. Shaulov, Y. Wolfus, R. Prozorov, L. Burlachkov, Y. Yeshurun, D. Majer, E. Zeldov, H. Wühl, V. B. Geshkenbein, and V. M. Vinokur, Phys. Rev. Lett **77**, 1596 (1996)

[47] T. Giamarchi and P. Le Doussal, Phys. Rev. B **55**, 6577 (1997)

[48] A. E. Koshelev and V. M. Vinokur, Phys. Rev. **57**, 138026 (1998)

[49] V. Vinokur, B. Khaykovich, E. Zeldov, M. Konczykowski, R. A. Doyle, and P. H. Kes, Physica C **295** 209 (1998)

[50] E. Zeldov, D. Majer, M. Konczykowski, A. I. Larkin, V. M. Vinokur, V. B. Geshkenbein, N. Chikumoto, and H. Shtrikman, Europhys. Lett **30**, 367, (1995)

[51] C. D. Dewhurst, D. A. Cardwell, A. M. Campbell, R. A. Doyle, G. Balakrishnan, and D. McK. Paul, Phys. Rev. B **53**, 14594 (1996)

[52] F. Zuo, S. Khizroev, X. Jian, J. L. Peng and R. L. Greene, Phys. Rev. Lett. **72**, 1746 (1994)

[53] M. C. Andrade, N. R. Dilley, F. Ruess and M. B. Maple Phys. Rev. B **57** , R708 (1998)

[54] D. Giller, A. Shaulov, R. Prozorov, Y. Abulafia, Y. Wolfus, Y. Yeshurun, E. Zeldov, V. M. Vinokur, J. L. Peng, and R. L. Greene, Phys. Rev. Lett. **79**, 2542 (1997)

[55] C. D. Dewhurst and R. A. Doyle, Phys. Rev. B **56**, 10832 (1997)

[56] L. I. Glazman and A. E. Koshelev, Phys. Rev. B **43**, 2835 (1991)

[57] Cheng Zheng, P. L. Leath and S. Fisher, Phys. Rev. Lett. **82**, 1935 (1999)

[58] L. Burlachkov, V. B. Geshkenbein, A. E. Koshelev, A. I. Larkin , and V. M. Vinokur, Phys. Rev. B **50**, 16770 (1994)

[59] M. Nideröst, R. Frassanito, M. Saalfrank, A. C. Mota, G. Blatter, V. N. Zavaritsky, T. W. Li, and P. H. Kes, Phys. Rev. Lett. **81**, 3231 (1998)

[60] D. Majer, E. Zeldov, and M. Konczykowski, Phys. Rev. Lett. **57**, 1166 (1995)

[61] R. A. Doyle, S. F. W. R. Rycroft, T. B. Doyle, E. Zeldov, T. Tamegai, and S. Ooi, Phys. Rev. B **53** 135 (1998)

[62] Gianni Blatter and B. Ivlev, Phys. Rev. Lett. **72** 3867 (1994)

[63] A. Schilling, R.jin, J. D. Guo, and H. R. Ott, Phys. Rev. Lett **71**, 1899 (1993)

[64] L. W. Lombardo, D. B. Mitzi, and A. Kapitulnik, Phys. Rev. B **46** 5615 (1992)

[65] C. J. van der Beek and P. H. Kes, Phys. Rev B **43**, 13032 (1991)

[66] J. Yazyi, A. Arrbére, C. Durán, F. de la Cruz, D. B. Mitzi, and A. Kapitulnik, Physica C **184**, 254 (1991)

[67] F. Zuo, S. Khizroev, G. C. Alexandrakis, and V. N. Kopylov, Phys. Rev. B **52**, R755 (1995)

[68] P. W. Anderson, Phys Rev. Lett. **6**, 309 (1988) ; Y. B. Kim, C. F. Hempstead and A. R. Strnad, Phys. Rev. Lett. **9** (1962) 306.

[69] M.E. McHendry, S. Simizu, H. Lessure, M. P. Maley, J. Y. Coulter, I. Tanaka, H. Kojima, Phys. Rev. **44** (1991) 7614.

[70] F. Zuo and S. Khizroev, J.Appl.Phys. **76** (1994) 6953 (1994); L. Fabrega, J. Fontcuberta, S. Pinol Physica C **245** (1995) 325-331; D. Giller, Y. Abulafia, R. Prozorov, Y. Wolfus, A. Shaulov, Y. Yeshurun, D. Majer, E. Zeldov, J. L. Peng, R. L. Greene, Physica C **282-287** (1997) 2209; Y. Abulafia, D. Giller, Y. Wolfus, A. Shaulov, Y. Yeshurun, D. Majer, E. Zeldov, J. L. Peng, R. L. Greene, J. Appl. Phys. **81** (1997) 4944.

[71] V. Feigel'man, V. B. Geshkenbein, A. I. Larkin, and V. M. Vinokur, Phys. Rev. Lett. **63** (1989) 2303.

[72] L. Burlachkov, Phys. Rev. B **47** (1993) 8056.

[73] A. P. Malozemoff and M. P. A. Fisher, Phys. Rev. B **42** (1990) 6784.

[74] V. V. Metlushko, G. Güntherodt, V. V. Moshchalkov, and Y. Bruynseraede, Europhys. Lett. **26** (1994) 371.

[75] V. N. Zaravitsky and N. V. Zavaritsky, Physica C **185-189** (1991) 1887.

[76] M. Nideröst, A. Suter, P. Visani, A. C. Mota, G. Blatter, Phys. Rev. B **53** (1996) 9286.

[77] M. P. Maley, J. O. Willis, H. Lessure and M. E. McHenry, Phys. Rev. B **42** (1990) 2639.